Tuning the Multiferroic Properties of BiFeO$_3$ under Uniaxial Strain

P. Hemme,[1,2] J-C. Philippe,[1,3] A. Medeiros,[1,4] A Alekhin,[1] S. Houver,[1] Y. Gallais,[1] A. Sacuto,[1] A. Forget,[5]
D. Colson,[5] S. Mantri,[6] B. Xu,[7] L. Bellaiche,[6] and M. Cazayous[1]

[1]*Laboratoire Matériaux et Phénomènes Quantiques, Université Paris Cité, CNRS,*
10 rue Alice Domon et Léonie Duquet, 75205 Paris Cedex 13, France
[2]*Synchrotron SOLEIL, L'Orme des Merisiers Saint-Aubin, BP 48, 91192 Gif-sur-Yvette, France*
[3]*Laboratoire de Physique des Solides, CNRS, Université Paris-Saclay, 91405 Orsay, France*
[4]*Université Paris-Saclay, CNRS, Centre de Nanosciences et de Nanotechnologies, 91120, Palaiseau, France*
[5]*Service de Physique de l'Etat Condensé, CEA Saclay, IRAMIS, SPEC (CNRS URA 2464), F-91191 Gif sur Yvette, France*
[6]*Physics Department and Institute for Nanoscience and Engineering, University of Arkansas, Fayetteville, Arkansas 72701, USA*
[7]*Institute of Theoretical and Applied Physics, Jiangsu Key Laboratory of Thin Films, School of Physical Science and Technology,*
Soochow University, Suzhou 215006, China

More than twenty years ago, multiferroic compounds combining in particular magnetism and ferroelectricity were rediscovered. Since then, BiFeO$_3$ has emerged as the most outstanding multiferroic by combining at room temperature almost all the fundamental or applicative properties that may be desired: electroactive spin wave excitations called electromagnons, conductive domain walls, or a low band gap of interest for magnonic devices. All these properties have so far only been discontinuously strain engineered in thin films according to the lattice parameter imposed by the substrate. Here we explore the ferroelectricity and the dynamic magnetic response of BiFeO$_3$ bulk under continuously tunable uniaxial strain. Using elasto-Raman spectroscopy, we show that the ferroelectric soft mode is strongly enhanced under tensile strain and driven by the volume preserving deformation at low strain. The magnonic response is entirely modified with low energy magnon modes being suppressed for tensile strain above pointing out a transition from a cycloid to an homogeneous magnetic state. Effective Hamiltonian calculations show that the ferroelectric and the antiferrodistortive modes compete in the tensile regime. In addition, the homogeneous antiferromagnetic state becomes more stable compared to the cycloidal state above a +2% tensile strain close to the experimental value. Finally, we reveal the ferroelectric and magnetic orders of BiFeO$_3$ under uniaxial strain and how the tensile strain allows us to unlock and to modify in a differentiated way the polarization and the magnetic structure.

Bismuth ferrite (BiFeO$_3$-BFO) is one of the few single-phase multiferroic materials which has both ferroelectric and antiferromagnetic properties at room temperature [1,2,14]. BFO offers multifunctional properties such as a strong photostriction response [15], conductive domain walls [16], and low band gap, promising for spintronics [17,18], tunnel junction [19], and photovoltaics [20,21]. Beyond the fundamental aspect of their origin which in some cases still needs further clarification, such properties are interesting for future applications only if it is possible to modify them in a controlled way. Magnetic and electric fields, as well as chemical doping, can play that role [22–24]. Strain engineering appeared as a way to achieve efficiently the tuning of the various remarkable functionalities of perovskite oxides and to explore their phase diagrams [25]. Three-dimensional strains obtained in an anvil pressure cell and applied to BFO bulk are able to induce structural phase transitions and drive the magnetic order from a noncollinear to a homogeneous magnetic state

[26]. However, the spontaneous polarization of BFO disappears under hydrostatic pressure due to the appearance of the antipolar orthorhombic phase [27]. In BFO thin films, 2D epitaxial strains also drive the dynamic magnetic response [28] and can modify the bulklike spin cycloid [29]. In contrast with the behavior of standard ferroelectrics, the ferroelectric Curie temperature T$_C$ decreases dramatically with 2D epitaxial strain due to the interplay of oxygen octahedral tilts with ferroelectric displacements [30]. The magnitude of the overall polarization in BFO is constant under strain although compressive substrate strains lead to an increase of the out-of-plane component of polarization and a decrease of the in-plane components of polarization while tensile substrate strains have the opposite effect [31,32]. Since BFO has a very large polarization ($P = 100$ C/cm^2), it would be more promising to obtain an increase of the overall polarization toward its integration in memristors for example. On the other hand, although theoretical works have shown that a

uniaxial strain is able to modify the polarization of BFO and in particular increase it [33], experimental measurements are yet to corroborate it.

In this Letter, we study the ferroelectric and dynamic magnetic orders of BFO under continuously variable uniaxial strain using elasto-Raman scattering. The effect of uniaxial strain on vibrational modes shows that only the phonon modes at low frequencies of 70 and 75 cm^{-1} associated with the soft mode of the ferroelectric transition are modified by the strain $\epsilon_{[100]}$ up to 1.5%. They show a quadratic variation at low strain and a deviation from this quadratic behavior at higher strain. In addition, the increase of the soft mode intensity under tensile strain is correlated with the increase of the polarization calculated using effective Hamiltonian simulations and with the intensity of a specific magnon mode with a polar activity called an electromagnon. Our calculations demonstrate that the ferroelectric and the antiferrodistortive modes compete with each other in the tensile strain regime. Measurements and calculations show that the [1-10] cycloid is always more stable until the strain induces the modifications of the spin excitations and drives the transition from a noncollinear to a homogeneous antiferromagnetic (AFM) state. The different effect of the uniaxial strain on the polarization and spin modes allows us to consider a differential use of the uniaxial strain on ferroelectric and magnetic properties.

We explored the ferroelectric and magnetic phase diagram of BFO at room temperature combining confocal Raman spectroscopy and a uniaxial piezoelectric cell described in Fig. 1(a) and in the Supplemental Material. There are two important points to note. First, unlike most deformation techniques which are performed under constant uniaxial strain, the setup involved in this Letter is able to apply *in situ* to both tensile and compressive strains along a given direction. Second, the BFO monocrystals have been cut and oriented so that the strain is applied along [100] in the pseudocubic direction. This direction corresponds to the projection of the [111] polarization direction on the (110) top face of the BFO single crystal. The strain cell is equipped with a capacitor sensor which monitors *in situ* the change δL in the gap between the two moving sample plates. It gives access to the nominal strain applied to the crystal along the [100] direction: $\epsilon_{[100]} = \delta L/L_0$ with L_0 the unstrain length of the gap.

Figure 1(b) shows the phonon modes of a BiFeO$_3$ single crystal measured at room temperature in the 60–85 cm^{-1} range from compressive ($\epsilon_{[100]} = -1.6\%$) to tensile strain ($\epsilon_{[100]} = +1.5\%$). Only these two phonon modes present a change in their energies (Raman shift). The width of these peaks remains constant under strain which indicates that the strain is applied in a homogeneous way. The vibrational spectra of BFO are well characterized by Raman [34,35], infrared [36,37], and lattice dynamical calculations [38,39] that converge to a common description of phonon modes.
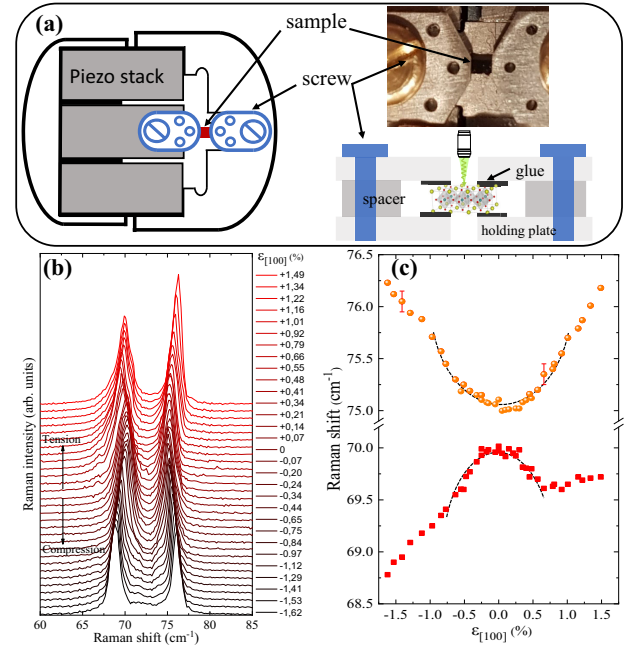

FIG. 1. (a) Schematic of the uniaxial strain application system seen from below (piezoelectric stack) as well as an enlarged picture of the strain setup and a schematic of a cross section showing how the sample is fixed ([2]). (b) Phonon spectra measured for several compressive and tensile strains inside the pressure cell. (c) Raman shift of the phonon modes at 70 and 75 cm^{-1} [13]. The dashed lines are a quadratic guide for the eye.

In particular, the phonon mode at 75 cm^{-1} with a E symmetry is responsible for the temperature dependence of the dielectric constant and is the leading candidate to be the soft mode of the ferroelectric transition [36,37].

Figure 1(c) gives the dependence of both the phonon energies as a function of strain. Compressive and tensile strains lead to the symmetric hardening (frequency upshift) of the 75 cm^{-1} phonon energy. At low strain the energy of this peak has a variation close to ϵ^2 up to $\pm 1\%$ while the variation deviates from this quadratic behavior at higher strain. The energy of the phonon at 70 cm^{-1} presents also a quadratic downshift under low compressive and tensile strain up to $\pm 0.7\%$. What is notable is the anomaly at $+0.7\%$ with a variation of the energy almost equal to zero at higher tensile strain.

Figure 2(a) shows the low-energy part of the Raman spectra obtained for several strains. The series of narrow peaks are the Raman fingerprint of the cycloidal spin excitations (magnons) at zero wave vector and have also been evidenced by Thz spectroscopy [40–42]. They correspond to cyclon ($\phi_{0,1,...}$) and extra-cyclon ($\psi_{0,1,...}$) modes (following the notation in Ref. [43]) associated with oscillations in and out of the cycloid plane, respectively. According to the Ginsburg, Landau, and Hamiltonian models that have been developed to account for these modes, their microscopic origins lie in Dzialoshinskii-Moriya interactions and easy-axis anisotropy [44].
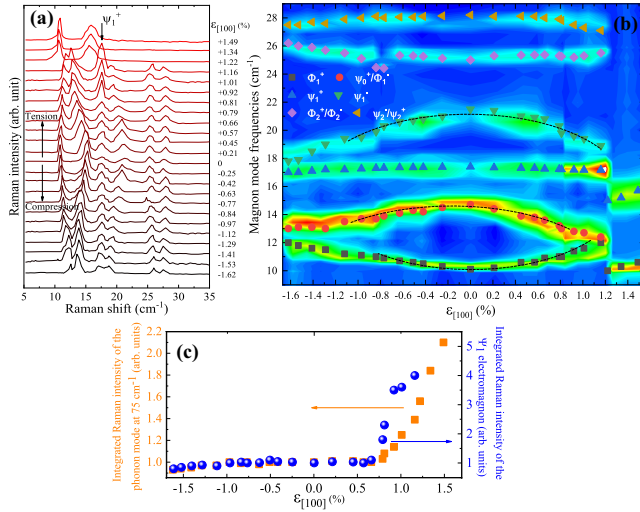
FIG. 2. (a) Low energy part of Raman spectra showing the spin excitations under the applied strain. (b) Magnon mode frequencies and 2D color map of the Raman intensity (color scale) as a function of the deformation $\epsilon_{[100]}$. (c) Comparison of the strain dependence between the integrated Raman intensity of the ψ_1^+ magnon mode and of the phonon mode at 75 cm^{-1}.

Among all these modes, the peak around 17 cm^{-1} identified as the ψ_1^+ mode has been suspected to be an electroactive magnetic excitation called an electromagnon [43]. Figure 2(a) shows the shift of the modes and the replacement of the series of peaks by only two peaks above $\epsilon_{[100]} = +1.2\%$.

Figure 2(b) depicts the corresponding spin excitation energies as a function of $\epsilon_{[100]}$. The superimposed color map represents the associated intensity of the modes. Some spin excitations harden while others soften with a tendency for the modes to merge at high strain. The modes at 10 and 14 cm^{-1} show a shift close to a quadratic variation over a larger strain range than the one observed for the phonon modes. Above $\epsilon_{[100]} = +1.16\%$, only two spin excitations are observed. This change signals the sudden disappearance of the spin cycloid and the transition to a homogeneous antiferromagnetic order. The color map shows that the intensity of the spin modes is almost constant over the range of strain except for the ψ_1^+ mode at 17 cm^{-1} that shows a noticeable increase in its intensity under tensile strain above $\epsilon_{[100]} = +0.75\%$.

In addition, we compare the response of phonons and spin waves under strain. In Fig. 2(c), the integrated Raman intensities of the ψ_1^+ spin mode and of the phonon mode at 75 cm^{-1} are plotted as a function of $\epsilon_{[100]}$. The evolutions are soft with a small decrease (increase) under compression (tension) strain between -1.5% and -0.7%. Above a tension of $\epsilon_{[100]} = +0.8\%$, both the phonon and spin mode intensities abruptly increase. Remember that the ψ_1^+ spin mode is an electromagnon and the phonon mode at 75 cm^{-1} is the soft mode driving the ferroelectric

transition. Figure 2(c) shows a clear correlation between both as expected if the electroactivity of the electromagnon comes from the soft phonon of the ferroelectricity. The abrupt increase of the ψ_1^+ magnon and of the phonon at 75 cm^{-1} intensities around $\epsilon_{[100]} = +0.8\%$ might indicate at first glance that the ferroelectricity mode is affected by the magnetic transition. Note that this change occurs around the same strain value as the anomaly in the phonon frequency at 70 cm^{-1} and the observed deviation from the quadratic behavior for the frequency of the phonon mode at 75 cm^{-1} in Fig. 1(c). These three changes are concomitant in strain but significantly below the magnetic transition observed around $+1.2\%$. This indicates that the transition in the ferroelectric soft mode at 0.8% is not related to the magnetic transition.

Assuming we can neglect the deformation perpendicular to the plane of the sample in which the [100] uniaxial strain is applied, we have to consider the deformation along both of the in-plane components, i.e., [010] and [100] directions. The strain comes from two sources: the isotropic distortion ϵ_{ISO} ($\epsilon_{[100]} = \epsilon_{[010]}$) and the volume-preserving anisotropic distortion ϵ_{AS} ($\epsilon_{[100]} = -\epsilon_{[010]}$). For small strain, ϵ_{ISO} gives a linear strain response at the first order whereas ϵ_{AS} induces a square strain response. In a simplified way, we can link the variation of the Raman mode frequency Δ_ω to these two terms: $\Delta_\omega = \alpha\epsilon_{\mathrm{AS}}^2 + \beta\epsilon_{\mathrm{ISO}} + \gamma\epsilon_{\mathrm{ISO}}^2$ in which α, β, and γ are coefficients. The last term corresponds to the second order of the isotropic distortion whose contribution is expected to be negligible compared to the other two. The in-plane Poisson's ratio for BFO is about 0.40 which means that about 30% of the strain along [100] comes from the isotropic distortion and 70% from the volume-preserving distortion. We therefore expect that the structural and magnetic changes are driven by the anisotropic distortion (volume-preserving) and as a result the energy of the modes should present a quadratic shift with compressive and tensile strain.

Indeed, the phonon energies at 75 cm^{-1} and 70 cm^{-1} show quadratic and symmetric variation at low strain in Fig. 1(c) suggesting that volume preserving distortion is the dominant mechanism at low strain. At higher strain, the energy shift of the both phonons deviates from the quadratic behavior. The second component to the deformation, i.e., the isotropic distortion, may no longer be negligible. Spin excitations show a less clear behavior. However, the spin modes at low energies [10 and 14 cm^{-1} in Fig. 2(b)] present a variation close to a quadratic shift over a large strain range.

In order to shed light on the behavior of structural and magnetic orders with strain, Monte Carlo simulations using a first-principles-based effective Hamiltonian for bulk BFO (detailed in Refs. [45,46] and in the Supplemental Material) were carried out. The strain is calculated with respect to the lattice parameter of bulk BFO in the $R3c$ phase calculated from first principles at 0.1 K. The most important structural
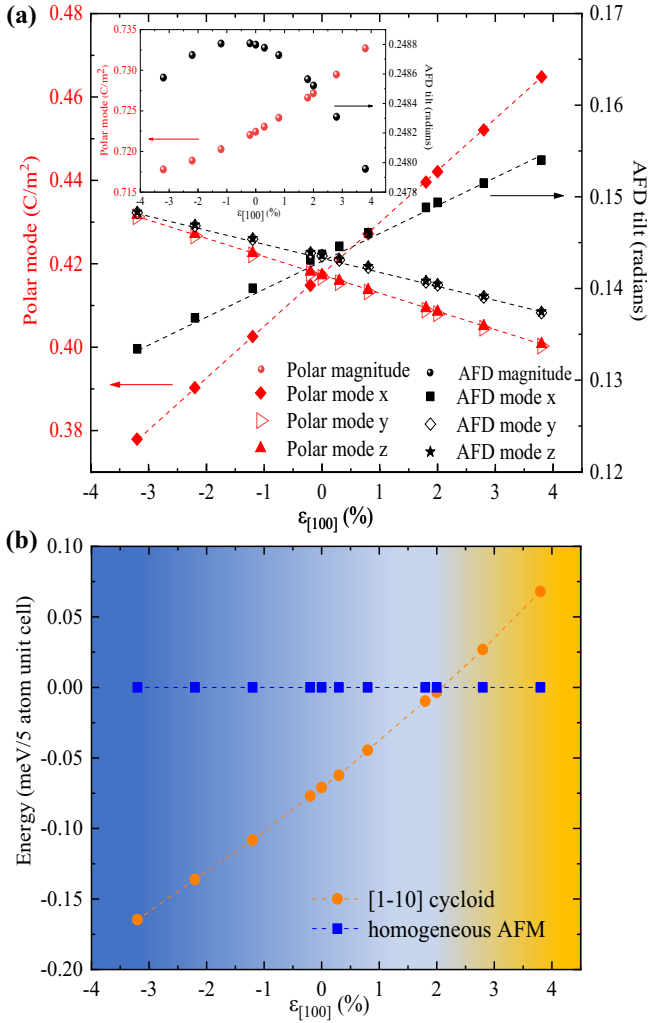
FIG. 3. (a) Evolution of the polarization and AFD mode components along [100], [010], and [001] directions under [100] oriented tensile and compressive strain. The AFD components along the x, y, and z direction represent the antiphase tilts in radians about the x, y, and z axes. The inset shows the polarization and AFD tilt magnitudes. (b) Energy comparison of relaxed bulk BFO with two magnetic spin configuration: type I spin cycloid state with propagation vector along [1-10] and homogeneous G-type AFM state.

quantities in the BFO $R3c$ phase are the polarization related to local modes and the tilting of oxygen octahedra related to the antiferrodistortive (AFD) pseudovectors. Figure 3(a) shows the change in polarization (C/m²) and AFD modes (radians) with strain. In its bulk form, BFO has polarization and oxygen octahedra tilt oriented along the [111] direction. Note that the maximum of the polar mode versus strain does not occur at 0 strain. For compressive strain, the y and z components of the polarization are slightly enhanced, while for tensile strain it is the x components that are strongly enhanced. However, as the tensile (compressive) strain along [100] increases, the component of the polarization along the [100] direction (polar mode x)

increases (decreases) while the component of the polarization along both [010] (polar mode y) and [001] (polar mode z) decreases (increases). The polarization magnitude increases as the tensile strain increases, while it decreases with the compressive strain, as can be seen from the inset in Fig. 3(a). Under the tensile strain, the oxygen octahedron rotates towards the [100] axis [as shown by the increase of the x component of the AFD mode in Fig. 3(a)] from the traditional [111] axes, while under compressive strain, it rotates towards the [011] axis [as shown by the increase of the y and z components of the AFD mode in Fig. 3(a)]. The AFD magnitude decreases with increasing compressive as well as tensile strain [as can be seen in the inset of Fig. 3(a)]. BFO is in the monoclinic Cc phase (space group symmetry number 9) all across the compressive and tensile strain range studied. A comparison of the FE and AFD magnitude shows that the two modes compete with each other in the tensile strain range.

Notice that, in the inset of Fig. 3(a), the polarization value in the AFM region is about 0.725 C/m² at +1.2% and increases up to 0.732 C/m² around 4%, representing an increase of 1% of the electric polarization value. Dong *et al.* calculated that the electric polarization under a uniaxial strain along the [111] direction of the polarization increases 5% for a 4% tensile strain [33]. This higher increase compared to our Letter illustrates the fact that we did not experimentally apply the strain in the direction of polarization. From an experimental point of view, it was not possible to simultaneously perform the polarization and optical measurements during the application of the strain simultaneously the measurements of the polarization and the optical measurements.

The structural simulation of Fig. 3(a) supports the experimental decrease of the FE soft mode intensity [Fig. 2(c)] under compressive strain and its increase under tensile strain. One should notice that a direct comparison between the soft mode and polarization cannot be made as one is dynamic and other is a static calculation. However, the calculations are not able to account for the jump in the intensity of the ferroelectric soft mode. It is important to underline that although there are no volume conditions imposed in our simulations, the volume did not change much during the Monte Carlo simulations. This means that in our simulations, it is the volume-preserving deformation that is at work. This disagreement is understandable since the jump corresponds experimentally to a deviation from the quadratic behavior and could indicate the more important role of the isotropic deformation at higher strain.

Using the effective Hamiltonian, we also studied the G-type AFM states and spin cycloids (only type I cycloids with propagation vector along [1-10], [10-1], and [01-1] were studied here). It is important to note here that the polar mode and its changes are nearly independent of which magnetic state is stable. It was found that the type I cycloid with a propagation vector along [1-10] was always more

stable than the other two cycloids with a propagation vector along [10-1] and [01-1]. We therefore present only the calculations concerning this cycloid. Figure 3(b) shows the comparison between the energies of the G-type AFM state and the [1-10] spin cycloid in the strain range -3% to $+4\%$. All through the compressive strain range and up to small tensile strain, the favorable magnetic state is the spin cycloid. A switch from the cyloidal magnetic state to the homogeneous G type AFM state occurs above $+2\%$. Compared to the calculated magnetic structure, the experimental results of Fig. 2(b) show that the AFM state is also reached under tensile strain of $+1.2\%$. The transition values are in the same order of magnitude. The difference can be explained by the fact that the simulations have been done at 0.1 K to be able to compute the free energy (as it is the internal energy at such low temperature), while the experiments were done at 300 K. The good agreement between experimental measurements and simulations obtained for the magnetic order indicates that, unlike phonons, spin waves remain mostly driven by the 1D deformation (volume preserving deformation) over the whole strain range.

In Ref. [26], the authors measured the magnetic excitations of BFO under hydrostatic pressure. At the first structural transition, the magnetic cycloid vanishes and a homogeneous AFM order sets in. Calculations show that the anisotropy and the angle between the FE polarization and the AFD vector drive the magnetic transition with pressure. In this Letter, the magnetic transition is not associated with a structural transition. In addition, the main effect of the uniaxial deformation is via its volume preserving component even if the isotropic component plays a role at higher strain. The term that is mostly responsible for the cycloid is the spin-current term, which is of the form $(P \times e_{ij}).(m_i \times m_j)$ where e_{ij} is the unit vector from site i to site j. It is stronger when P is perpendicular to e_{ij} (e.g., polarization P along [111] and e_{ij} along [−110] for the $\langle -110\rangle$-type cycloid) and becomes smaller when P goes towards e_{ij}. If the angle between P and e_{ij} deviates from 90° more and more with strain, then the cycloid decreases its energy more and more with respect to that of the AFM state.

Tensile uniaxial strain applied along the [100] axis significantly increases the polarization (this increase would probably be even more with a strain directly along the [111] polarization axis). Photovoltaic applications can benefit from such an enhancement. Indeed, both the BFO optical absorption (through the reduction of the optical band gap) and the photocurrent (proportional to the polarization amplitude) should contribute to the increase of the photovoltaic efficiency. In our measurements, the magnetic state transits from a cycloidal to a AFM state under tensile strain while the polarization increases simultaneously. This differentiation in the ferroelectric and magnetic response to the same strain can be exploited. A low uniaxial strain is thus able to unlock the spin cycloid from the polarization. As it has been done in thin films [28] but not continuously (the epitaxial misfit is a discrete parameter strain), we can modify the spin configuration of the antiferromagnetic state while independently controlling the ferroelectric order using an additional electric field.

In summary, we have combined elasto-Raman spectroscopy with effective Hamiltonian calculations to establish the diagram of the ferroelectric and antiferromagnetic phases of $BiFeO_3$ under uniaxial strain. While compressive strain decreases the polarization, tensile strain significantly increases the polarization in cross correlation with the increase of the activity of the electromagnon. The polarization in the tensile strain regime is governed by the competition between the ferroelectric and the antiferrodistortive modes. We observe the complete quench of high energy magnon modes with tensile strain associated with the disappearance of the spin cycloid and the transition to a homogeneous antiferromagnetic state in agreement with calculations. The ferroelectric soft mode experiences a deformation which is no longer totally quadratic (volume preserving) at high strain in contrast to the magnetic state. The unlocking of the spin excitations from the polarization that simultaneously increases has interesting implications for the implementation of uniaxial strained BFO in magnonic and spintronic devices.

[1] D. Lebeugle, D. Colson, A. Forget, M. Viret, P. Bonville, J. F. Marucco, and S. Fusil, Phys. Rev. B **76**, 024116 (2007).

[2] See Supplemental Material at http://link.aps.org/supplemental/10.1103/PhysRevLett.131.116801 for the description of BFO properties, which includes Refs. [3–10]; for the description of the setup which includes Refs. [11–13].

[3] J. R. Teague, R. Gerson, and W. J. James, Solid State Commun. **8**, 1073 (1970).

[4] J. B. Neaton, C. Ederer, U. V. Waghmare, N. A. Spaldin, and K. M. Rabe, Phys. Rev. B **71**, 014113 (2005).

[5] P. Ravindran, R. Vidya, A. Kjekshus, H. Fjellvåg, and O. Eriksson, Phys. Rev. B **74**, 224412 (2006).

[6] I. Sosnowska, T. Neumaier, and E. Steichele, J. Phys. C **15**, 4835 (1982).

[7] M. Matsuda, R. S. Fishman, T. Hong, C. H. Lee, T. Ushiyama, Y. Yanagisawa, Y. Tomioka, and T. Ito, Phys. Rev. Lett. **109**, 067205 (2012).

[8] J. Lee, I. Kézsmàki, and R. Fishman, New J. Phys. **18,** 043025 (2016).

[9] M. Ramazanoglu, M. Laver, W. Ratcliff, S. M. Watson, W. C. Chen, A. Jackson, K. Kothapalli, S. Lee, S. W. Cheong, and V. Kiryukhin, Phys. Rev. Lett. **107,** 207206 (2011).

[10] C. W. Hicks, M. E. Barber, S. D. Edkins, D. O. Brodsky, and A. P. Mackenzie, Rev. Sci. Instrum. **85,** 065003 (2014).

[11] J.-C. Philippe, J. Faria, A. Forget, D. Colson, S. Houver, M. Cazayous, A. Sacuto, and Y. Gallais, Phys. Rev. B **105,** 024518 (2022).

[12] J. M. Bartlett, A. Steppke, S. Hosoi, H. Noad, J. Park, C. Timm, T. Shibauchi, A. P. Mackenzie, and C. W. Hicks, Phys. Rev. X **11,** 021038 (2021).

[13] F. Lin, R. J. Bodnar, and S. P. Becker, Geochim. Cosmochim. Acta **71,** 3746 (2007).

[14] G. Catalan and J. F. Scott, Adv. Mater. **21,** 2463 (2009).

[15] B. Kundys, M. Viret, D. Colson, and D. O. Kundys, Nat. Mater. **9,** 803 (2010).

[16] J. Seidel, L. W. Martin, Q. He, Q. Zhan, Y.-H. Chu, A. Rother, M. E. Hawkridge, P. Maksymovych, P. Yu, M. Gajek, N. Balke, S. V. Kalinin, S. Gemming, F. Wang, G. Catalan, J. F. Scott, N. A. Spaldin, J. Orenstein, and R. Ramesh, Nat. Mater. **8,** 229 (2009).

[17] J. Dho, X. Qi, H. Kim, J. L. MacManus-Driscoll, and M. G. Blamire, Adv. Mater. **18,** 1445 (2006).

[18] J. Allibe, S. Fusil, K. Bouzehouane, C. Daumont, D. Sando, E. Jacquet, C. Deranlot, M. Bibes, and A. Barthélémy, Nano Lett. **12,** 1141 (2012).

[19] H. Béa, M. Bibes, S. Cherifi, F. Nolting, B. Warot-Fonrose, S. Fusil, G. Herranz, C. Deranlot, E. Jacquet, K. Bouzehouane, and A. A. Barthélémy, Appl. Phys. Lett. **89,** 242114 (2006).

[20] T. Choi, S. Lee, Y. J. Choi, V. Kiryukhin, and S.-W. Cheong, Science **324,** 63 (2009).

[21] R. Guo, L. You, Y. Zhou, Z. Shiuh Lim, X. Zou, L. Chen, R. Ramesh, and J. Wang, Nat. Commun. **4,** 1990 (2013).

[22] M. Tokunaga, M. Akaki, T. Ito, S. Miyahara, A. Miyake, H. Kuwahara, and N. Furukawa, Nat. Commun. **6,** 5878 (2015).

[23] V. A. Khomchenko, D. A. Kiselev, J. M. Vieira, L. Jian, A. L. Kholkin, A. M. L. Lopes, Y. G. Pogorelov, J. P. Araujo, and M. Maglione, J. Appl. Phys. **103,** 024105 (2008).

[24] P. Rovillain, R. de Sousa, Y. Gallais, A. Sacuto, M. A. Méasson, D. Colson, A. Forget, M. Bibes, A. Barthélémy, and M. Cazayous, Nat. Mater. **9,** 975 (2010).

[25] D. G. Schlom, L.-Q. Chen, C.-B. Eom, K. M. Rabe, S. K. Streiffer, and J.-M. Triscone, Annu. Rev. Mater. Res. **37,** 589 (2007).

[26] J. Buhot, C. Toulouse, Y. Gallais, A. Sacuto, R. de Sousa, D. Wang, L. Bellaiche, M. Bibes, A. Barthélémy, A. Forget, D. Colson, M. Cazayous, and M.-A. Measson, Phys. Rev. Lett. **115,** 267204 (2015).

[27] D. P. Kozlenko, A. A. Belik, A. V. Belushkin, E. V. Lukin, W. G. Marshall, B. N. Savenko, and E. Takayama-Muromachi, Phys. Rev. B **84,** 094108 (2011).

[28] A. Haykal, J. Fischer, W. Akhtar, J.-Y. Chauleau, D. Sando, A. Finco, F. Godel, Y. A. Birkhölzer, C. Carrétéro, N. Jaouen, M. Bibes, M. Viret, S. Fusil, V. Jacques, and V. Garcia, Nat. Commun. **11,** 1704 (2020).

[29] D. Sando et al., Nat. Mater. **12,** 641 (2013).

[30] I. C. Infante, S. Lisenkov, B. Dupé, M. Bibes, S. Fusil, E. Jacquet, G. Geneste, S. Petit, A. Courtial, J. Juraszek, L. Bellaiche, A. Barthélémy, and B. Dkhil, Phys. Rev. Lett. **105,** 057601 (2010).

[31] H. W. Jang, S. H. Baek, D. Ortiz, C. M. Folkman, R. R. Das, Y. H. Chu et al., Phys. Rev. Lett. **101,** 107602 (2008).

[32] C. Daumont et al., J. Phys. Condens. Matter **24,** 162202 (2012).

[33] H. Dong, Z. Wu, F. Wu, and J. Li, Phys. Status Solidi **12,** 1700431 (2018).

[34] M. Cazayous, D. Malka, D. Lebeugle, and D. Colson, Appl. Phys. Lett. **91,** 71910 (2007).

[35] C. Beekman, A. A. Reijnders, Y. S. Oh, S. W. Cheong, and K. S. Burch, Phys. Rev. B **86,** 020403(R) (2012).

[36] S. Kamba, D. Nuzhnyy, M. Savinov, J. Šebek, J. Petzelt, J. Prokleška, R. Haumont, and J. Kreisel, Phys. Rev. B **75,** 024403 (2007).

[37] R. P. S. M. Lobo, R. L. Moreira, D. Lebeugle, and D. Colson, Phys. Rev. B **76,** 172105 (2007).

[38] P. Hermet, M. Goffinet, J. Kreisel, and P. Ghosez, Phys. Rev. B **75,** 220102(R) (2007).

[39] H. M. Tütüncüa and G. P. Srivastavab, J. Appl. Phys. **103,** 083712 (2008).

[40] M. Cazayous, Y. Gallais, A. Sacuto, R. de Sousa, D. Lebeugle, and D. Colson, Phys. Rev. Lett. **101,** 037601 (2008).

[41] D. Talbayev, S. A. Trugman, S. Lee, H. T. Yi, S.-W. Cheong, and A. J. Taylor, Phys. Rev. B **83,** 094403 (2011).

[42] M. Bialek, T. Ito, H. Ronnow, and J. P. M. Ansermet, Phys. Rev. B **99,** 064429 (2019).

[43] R. S. Fishman, J. T. Haraldsen, N. Furukawa, and S. Miyahara, Phys. Rev. B **87,** 134416 (2013).

[44] D. G. Farkas et al., Phys. Rev. B **104,** 174429 (2021).

[45] S. Prosandeev, D. Wang, W. Ren, J. Íñiguez, and L. Bellaiche, Adv. Funct. Mater. **23,** 234 (2015).

[46] B. Xu, B. Dupé, C. Xu, H. Xiang, and L. Bellaiche, Phys. Rev. B **98,** 184420 (2018).